Journal of the Korean Society for Nondestructive Testing
Vol. 26, No. 3 (2006. 6)

Generation of Thermoelastic Waves by Irradiating a Metal Slab with a Line-Focused Laser Pulse

Jaegwon Yoo*,† and S. H. Baik*

Abstract A 2D finite-element numerical simulation has been developed to investigate the generation of ultrasonic waves in a homogeneous isotropic elastic slab under a line-focused laser irradiation. Discussing the physical processes involved in the thermoelastic phenomena, we describe a model for the pulsed laser generation of ultrasound in a metal slab. Addressing an analytic method, on the basis of an integral transform technique, for obtaining the solutions of the elastodynamic equation, we outline a finite element method for a numerical simulation of an ultrasonic wave propagation. We present the numerical results for the displacements and the stresses generated by a line-focused laser pulse on the surface of a stainless steel slab.

Keywords: Laser Ultrasonic, Thermoelastic Wave, Rayleigh Surface Wave, Elastodynamics, Finite Element Method

1. Introduction

Laser-based ultrasonics has several advantages in nondestructive testing and evaluation (NDT&E) over many conventional transducers, such as the ability to achieve a broad-banded excitation with a high signal reproducibility and the possibility of generating a truly remote source of ultrasound by optical means on hot or rough samples and in hostile environments. The characteristics of laser-based ultrasonic waves depend strongly on the optical penetration, the thermal diffusion, the elastic properties, and the geometry of materials, as well as the parameters of the exciting laser pulse, including the shape, the focus spot, and the pulse width (Scruby and Drain, 1990). In conjunction with NDT&E, the laser-generated ultrasound also has many industrial applications in the areas of laser ultrasonic velocity and attenuation measurements to determine the elastic constants and grain sizes of materials.

A number of different physical processes may take place when a solid surface is illuminated by a laser pulse. Typically, there are two regions for a laser generation of an ultrasound in a solid: thermoelastic (typical power densities $<10^7\ W/cm^2$ for a metal in the near infrared/visible wavelength region) and ablative (typical power densities $>10^7\ W/cm^2$ for a metal in the near infrared/visible wavelength region). In the thermoelatic region, a low-energy laser pulse heats the surface of the material, and the transient thermal expansion of the near surface volume launches the compression, shear, and Rayleigh waves into the sample. In the ablative region, on the other hand, a higher energy density laser pulse yields a partial ablation of the target surface and an ionization of the ablative material. The laser-induced plasma expands away from the surface with very high pressures so as to enhance the generation of the compression and Rayleigh waves in this region. However, the ablative region's production of an ultrasound results in some surface damage, which

Received: May 10, 2006, Accepted: May 23, 2006. * Laboratory for Quantum Optics, Korea Atomic Energy Research Institute, Daejon 305-353, Korea † Corresponding author: jgyoo@kaeri.re.kr

may make it inappropriate for a use in certain applications.

Recently, on the basis of integral transform methods, we studied the analytic solutions of the transient elastodynamic equations to obtain the time domain displacements and stresses of a sample surface. We developed a numerical analysis formulation to simulate the generation of thermoelastic surface waves in a homogeneous isotropic elastic half-space under a line-focused laser irradiation (Yoo et al., 2006), where the inverse transforms are numerically calculated. However, it turned out that the analytical approach is hopelessly difficult to apply in the case of complex geometries, even in the simple case of a slab, because it demands numerical evaluations of the multiple integrations. Since it is well-known that the finite element method (FEM) (Ludwig and Lord, 1988; Kishore et al., 2000; Zerwer et al., 2003) is much more suitable in dealing with arbitrary shapes than other numerical methods, we carried out numerical simulations based on the 2-dimensional finite element method to investigate the generation and propagation of ultrasonic waves in a metal slab.

2. Theoretical Formulation

At lower incident powers of the laser pulse, the physical processes include a heating and the generation of thermal and elastic waves in a material. For the thermal process, a classical thermal diffusion equation implies that the heat disturbance can propagate with an infinite propagation velocity. Since such a behavior is physically unacceptable, we introduce a hyperbolic equation of a heat transport with a resulting finite speed of heat propagation (typically somewhat larger than the longitudinal wave speed c_1). The latter feature provides a confidence that no unphysical behavior is being introduced by using the classical thermoelasticity, with its associated "infinite" speed of a heat propagation, though no appreciable effect on the numerical results has been found; it also allows for a simplification of certain analytical results (Yoo et al., 2006, 2005; Ozisik and Vick, 1984; Frankel et al., 1985).

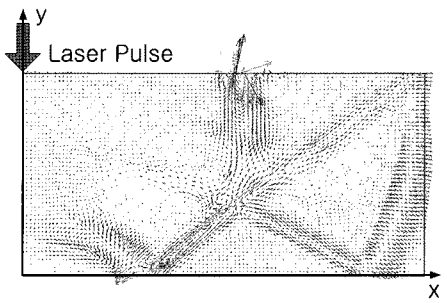

Fig. 1 Vector plots of the wavefronts radiating into the SUS316L slab at $t=1\,\mu s$. Note that only the right half part from the laser irradiation point is shown.

We consider a finite slab-type target that is composed of a medium with constant thermal properties and insulated boundaries. From time $t=0$, the medium is irradiated by a laser pulse depositing heat on its front surface. The hyperbolic time-dependent thermal diffusion equation for the temperature θ is written as

$$\nabla^2\theta-\frac{1}{\kappa}\frac{\partial\theta}{\partial t}-\frac{1}{c_1^2}\frac{\partial^2\theta}{\partial t^2}=-\frac{q}{k}, \tag{1}$$

where q is the heat source due to the laser irradiation, and the parameters involved in the thermal process are listed in Table 1. The medium in which the elastic pulses are generated is assumed to be homogeneous and isotropic. For an isotropic elastic body under laser irradiation, the displacement u satisfies the elastodynamic equation:

$$\mu\nabla^2u+(\lambda+\mu)\nabla(\nabla\cdot u)=\rho\frac{\partial^2u}{\partial t^2}+\beta\nabla\theta, \tag{2}$$

where $\beta=(3\lambda+2\mu)\alpha$ is the thermoacoustic coupling constant. The stress tensor σ is related to the displacement by

$$\sigma=\lambda\nabla\cdot u\boldsymbol{I}+\mu(\nabla u+u\nabla)-\beta\boldsymbol{I}\Delta\theta, \tag{3}$$

where $\Delta\theta$ represents the temperature difference.

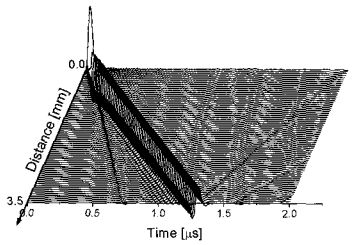

Fig. 2 Plot of the vertical displacement of the top surface of the SUS316L slab versus time. The distances measure the detection points from the center of the laser source.

In the Cartesian coordinates (x,y,z), a suitable expression for the heat deposition over the irradiation zone of the laser pulse is

$$q=E(1-R)\frac{e^{-y/\gamma}}{\gamma}f(x)g(t), \tag{4}$$

where E is the energy of the laser pulse per unit length, R is the surface reflectivity, and γ is the penetration depth. If the pulse energy is completely absorbed at the surface $(\gamma\to 0)$, we can set $e^{-y/\gamma}/\gamma=\delta(y)$. Here, $f(x)$ and $g(t)$ are the spatial and the temporal distributions of the laser pulse and they can be written as

$$f(x)=\frac{1}{\sqrt{2\pi}}\frac{2}{\varpi}e^{-2x^{2/\varpi^2}}, \tag{5}$$

$$g(t)=\frac{8t^3}{v^4}e^{-2t^{2/v^2}}, \tag{6}$$

where ϖ is the Gaussian width, and v is the pulse duration time of the laser beam.

The elastic displacement is obtained through a solution of the usual wave equations for the displacement potentials. The displacement vector u can be expressed in terms of a dilational scalar potential φ and an equivoluminal vector potential ψ as

$$u=\nabla\varphi+\nabla\times\psi. \tag{7}$$

Then, Eq. (2) will be satisfied if φ and ψ are solutions of the following wave equations:

$$\nabla^2\varphi-\frac{1}{c_1^2}\frac{\partial^2\varphi}{\partial t^2}=\frac{\beta}{c_1^2\rho}\theta, \tag{8}$$

$$\nabla^2\psi-\frac{1}{c_2^2}\frac{\partial^2\psi}{\partial t^2}=0, \tag{9}$$

where $c_1=\sqrt{(\lambda+2\mu)/\rho}$ and $c_2=\sqrt{\mu/\rho}$ are the speeds of the longitudinal and the transverse waves, respectively.

The elastodynamics involves the solution of boundary value problems with boundary conditions of the mixed type, in which the displacements are specified on one part of the boundary and those of the normal derivative on the remaining portion. For an insulated material, the boundary condition on the surface (S) of the medium is

$$n\cdot\nabla\theta(x,t)=0 \qquad \text{for } \mathbf{x}\in S, \tag{10}$$

and the initial conditions are

$$\theta(x,0)=\theta_0 \quad \text{and} \quad \frac{\partial\theta(\mathbf{x},0)}{\partial t}=0, \tag{11}$$

where n denotes a unit vector normal to the boundary surface S. The boundary conditions for the elastodynamic equations are such that the stresses are zero on the surface $(x\in S)$:

$$\sigma_{xy}=\mu\left(\frac{\partial u_y}{\partial x}+\frac{\partial u_x}{\partial y}\right)=0, \tag{12}$$

$$\sigma_{yy}=\lambda\left(\frac{\partial u_x}{\partial x}+\frac{\partial u_y}{\partial y}\right)+2\mu\frac{\partial u_y}{\partial y}-\beta\Delta\theta=0. \tag{13}$$

The initial conditions for the elastodynamic equFations are such that the displacements are zero at $t=0$.

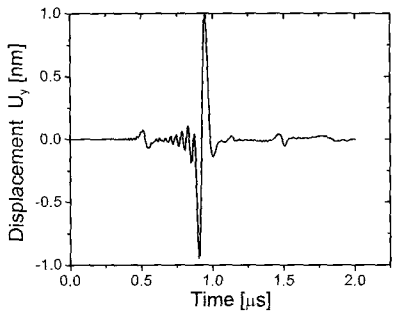

Fig. 3 Vertical displacement of the top surface of the SUS316L slab versus time at the distance 2.5 mm from the center of the laser source.

Since integral transforms may often reduce the partial differential equations to a simpler form, spatial Fourier and temporal Laplace transform methods are applied to the analysis and to the solutions of the boundary-value problems which involve a time dependence. The Fourier transform is the prototype of the most widely used class of unitary integral operators,

$$H(x,s)=\int_0^\infty h(x,t)e^{-st}dt. \tag{14}$$

The Laplace transformation is similarly designed to extend the advantages of a unitary transformation to a class of functions which are exponentially bounded,

$$\bar{H}(p,s)=\frac{1}{2\pi}\int_{-\infty}^{\infty}\int_{-\infty}^{\infty}H(x,s)e^{-ip\cdot x}dxdy. \tag{15}$$

Then, the integral transform of the line- focused laser source q reads

$$\bar{Q}=\frac{\beta E(1-R)}{k(\lambda+2\mu)}\bar{f}(p)G(s), \tag{16}$$

where G is the temporal Laplace transform of $g(t)$ and $\bar{f}$ is the spatial Fourier transform of $f(x)$,

$$\bar{f}=\frac{1}{2\pi}e^{-p^2\varpi^{2/8}}. \tag{17}$$

Successive applications of Eqs. (14) and (15) to the hyperbolic heat equation and the wave equations for the displacement potentials enable one to find the analytic solutions in the integral transformed form, i.e., in a multiple integral form of the displacements and stresses. However, it is almost impossible to obtain inversely transformed analytic solutions through multiple integral transforms, so the inverse transformations are usually calculated by using a numerical inverse method. Note that the integral of the inverse Fourier transform can be numerically evaluated by making use of Filon's method (Yoo et al., 2004; Abramowitz and Stegun, 1972), which is very adequate for rapidly oscillatory functions over semi-infinite intervals, and that the numerical inversion of the Laplace transform can be performed on the basis of the Crump-Durbin technique (Crump, 1976; Durbin, 1974).

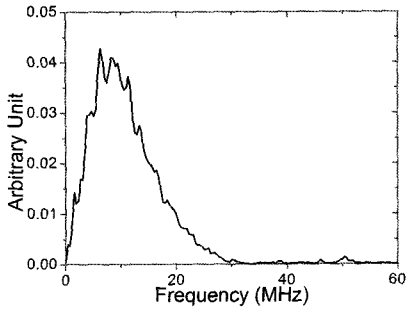

Fig. 5 Plot of spectrum of Fig. 5.

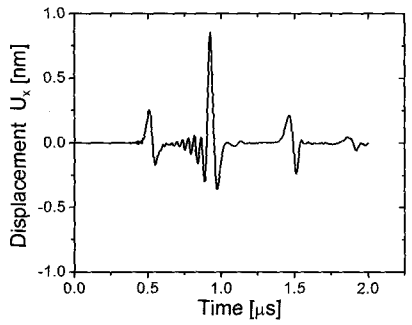

Fig. 4 Horizontal displacement of the top surface of the SUS316L slab versus time at the distance 2.5 mm from the center of the laser source.

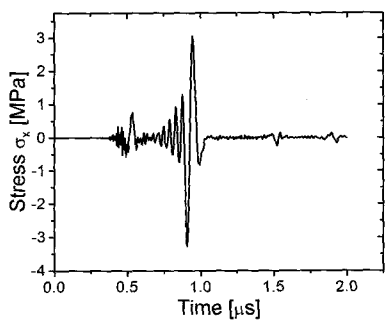

Fig. 6 Stress tensor σ_x at the top surface of the SUS316L slab versus time at the distance 2.5 mm from the center of the laser source.

3. Finite Element Method and Numerical Results

The numerical solution process based on the finite element method begins by meshing the region of interest into a set of simple geometrical elements such as triangles, rectangles, etc. The interiors of these elements are defined through approximation or shape functions in terms of displacement values at certain nodal points typically located along element boundaries. The nodal displacement values can be obtained by the minimization of the residue using Galerkin method (Burnett, 1987). This procedure reduces Eq. (2) to the following system of ordinary second-order linear differential equation,

$$[K]\{u\}+[M]\{\ddot{u}\}=\{F\}, \tag{18}$$

where $[K]$ is the stiffness matrix determined by the elastic properties of the medium, $[M]$ is the mass matrix determined by the density distribution of the medium and $\{F\}$ is the applied load vector. Since the form of Eq. (18) is identical to a simple mass-spring oscillator system, assembling all elements into a large global matrix system is equivalent to a solid consisting of discrete masses interconnected to one another by springs.

Numerical modelling based on the finite element method requires an appropriate mesh size and time increment according to the frequencies and wavelengths of interest. Note that large element size filters short wavelengths since the mesh plays a role of a low-pass filter. On the other hand, very small element size can cause numerical instability. In the wave propagation simulations, the numerical discretization errors associated with the element size can be minimized by using at least 10 nodes per minimum wavelength in the case of isotropic materials. For the minimum spatial resolution Δx, the time step can be estimated from $\Delta t=\Delta x/\sqrt{c_1^2+c_2^2}$ which is a condition that energy should not propagate right across a mesh volume in a single time-step. Moreover, boundary conditions and material properties must adequately represent the real situation.

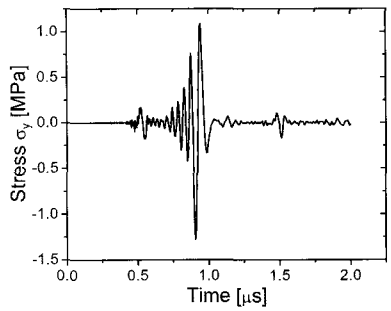

Fig. 7 Stress tensor σ_y at 25 μm below the top surface of the SUS316L slab versus time at the distance 25 mm from the center of the laser source.

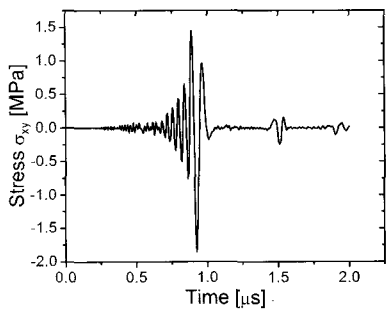

Fig. 8 Stress tensor σ_{xy} at 25 μm below the top surface of the SUS316L slab versus time at the distance 25 mm from the center of the laser source.

Table 1 Symbols of parameters and values of material constants for stainless steel (SUS316L)

	Parameter	SUS316L
c_1	Compression wave vel	5790 m/s
c_2	Shear wave velocity	3100 m/s
c_R	Rayleigh wave velocity	2870 m/s
ρ	Density	7960 kg/m^3
α	Linear expansion coeff.	$15.9\times10^{-6}\,K^{-1}$
κ	Thermal diffusivity	$2.5\times10^{-6}\,m^2/s$
k	Thermal conductivity	13.49 W/mK
R	Reflectivity	0.94 (@1.06 μm)
μ	Shear elastic modulus	78.6 GPa
λ	Lame elastic modulus	195.1 GPa
ν	Poisson ratio	0.293

We carried out the FEM simulations for thermoelastical generation of ultrasonic waves by the irradiation of a line-focused laser pulse on a stainless steel (SUS316L) slab. The overall dimensions of the SUS316L slab is 2.5 mm thick (y-direction) by 10 mm long (x-direction). The material parameters of SUS316L are listed in Table 1. The laser parameters are $E=1.8$ mJ per unit length, $\varpi=0.1$ mm and $\upsilon=30$ ns. The laser is focused on the center of the top surface of the slab. Since the laser specification is capable of generating ultrasonic waves having a central frequency of about 10 MHz, the minimum wavelength is around 29 μm. Accordingly we use the mesh size of 25 μm and the time step of 5 ns. To relieve computational burden of the computer system, we consider a 2-dimensional (with x- and y- axes) model which is legitimately employed in a system that has a symmetry about $y-z$ plane. Note that all the data plotted in the figures is computed at the distance 2.5 mm from the center of the laser source except for Figs. 1, 2 and 9.

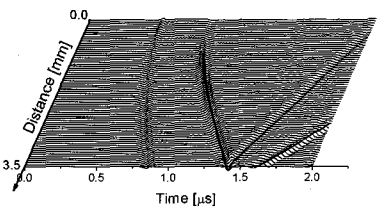

Fig. 9 Plot of the vertical displacement of the bottom surface of the SUS316L slab versus time. The distances measure the detection points from the center of the laser source.

A vector representation of the wavefronts radiating into the SUS316L slab at $t=1\,\mu$s is shown in Fig. 1, where only the right half part from the laser irradiation point is shown. Fig. 1 clearly shows that the compression, the shear and the head waves are propagating inside the slab and are being reflected at the bottom surface. On the top and bottom surface one can see the Rayleigh surface waves formed right before the shear wave parts.

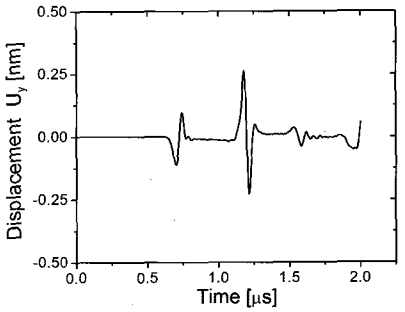

Fig. 10 Vertical displacement of the bottom surface of the SUS316L slab versus time at the distance 2.5 mm from the center of the laser source.

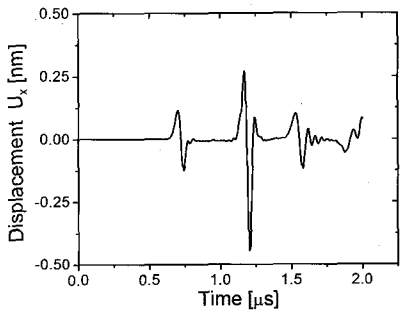

Fig. 11 Horizontal displacement of the bottom surface of the SUS316L slab versus time at the distance 2.5 mm from the center of the laser source.

Fig. 2 is a time-domain plot of the vertical displacement of the top surface of the slab, where the distances measure the detection points from the center of the laser source. Note that the time width of the ultrasonic pulse gets wider as the distance increases since the high frequency components suffer more severely from the attenuation than the low frequency components. The compression wave reflected from the corner of the top surface is barely seen in Fig. 2, where the reflected wavefront meets the shear wavefront at the distance 3.3 mm and is being mixed completely with the shear and Rayleigh wavefronts beyond this distance. Fig. 2 shows that another compression wavefront follows, which is reflected from the bottom surface.

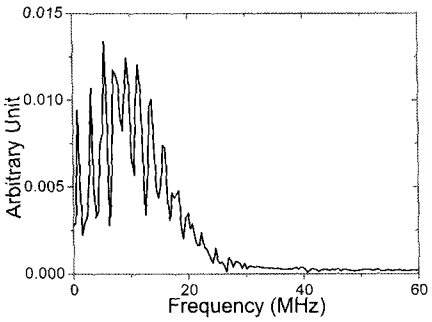

Fig. 12 Plot of spectrum of Fig. 13.

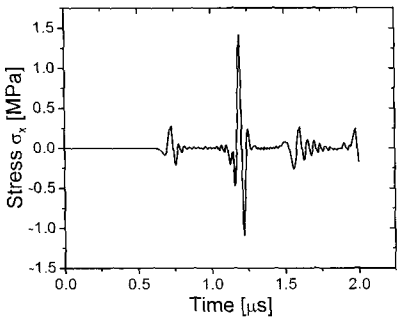

Fig. 13 Stress tensor σ_x at the bottom surface of the SUS316L slab versus time at the distance 2.5 mm from the center of the laser source.

Figs. 3 and 4 are the time-domain plots of the components u_y, u_x at the top surface, respectively. Figs. 3 and 4 show that there exist three distinct wave fronts, travelling with velocities c_1, c_2, and c_R, which are identified as the compression wave, the shear wave, and the Rayleigh surface wave, respectively. The central frequency of the ultrasonic wave of ~ 8MHz can be read from Fig. 5. The stress tensor component σ_x at the top surface of the slab is plotted in Fig. 6. The stress components σ_y and σ_{xy} at a position 25 μm below the top surface are computed and plotted in Figs. 7 and 8 because these stress tensor components are zero on the surface.

Before an arrival of the compression wave, u_y, σ_x, σ_y and σ_{xy} are completely quiescent as shown in Figs. 3, 4, 6, 7 and 8. At the arrival of the compression wave, u_y and σ_y begin to respond outwardly and σ_x toward the source. As the Rayleigh wave arrives, these values begin growing in opposite senses. The components of the shear wave are alleviated as the time becomes closer to the arrival of the Rayleigh wave while those of the Rayleigh wave have very large values right after the arrival of the Rayleigh wave. Note that the displacement of the Rayleigh surface wave decays much less than that of the compression wave with distance.

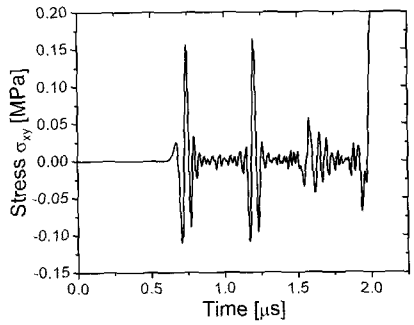

Fig. 14 Stress tensor σ_y at 25 μm above the bottom surface of the SUS316L slab versus time at the distance 2.5 mm from the center of the laser source.

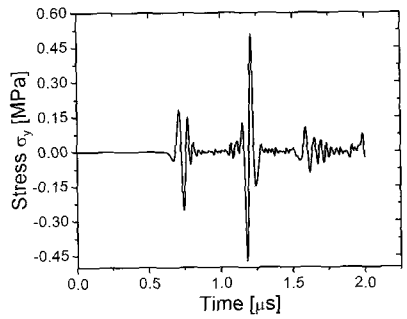

Fig. 15 Stress tensor σ_{xy} at 25 μm above the bottom surface of the SUS316L slab versus time at the distance 2.5 mm from the center of the laser source.

Fig. 9 is a time-domain plot of the vertical displacement of the bottom surface of the slab. Note that the distances measure the detection points from the center of the laser source. Also, Fig. 9 shows that the time width of the ultrasonic wave gets wider as the distance increases because

of the high frequency attenuation. The compression wave reflected from the corner of the bottom surface is clearly seen in Fig. 9, where the reflected wavefront meets the shear wavefront at the distance of 3.3mm and it is separated completely from the shear and Rayleigh wavefronts beyond this distance. Fig. 9 shows that other wavefronts are following, which are reflected from the top surface and from the corner of the bottom surface.

Figs. 10 and 11 are the time-domain plots of the components u_y, u_x at the bottom surface, respectively. Figs. 10 and 11 show that there three distinct wave fronts exist, travelling with velocities c_1, c_2, and c_R, which are identified as the compression wave, the shear wave, and the Rayleigh surface wave, respectively. The central frequency of the ultrasonic wave of $\sim 8\,\mathrm{MHz}$ can be read from Fig. 12. The stress tensor component σ_x at the bottom surface of the slab is plotted in Fig. 13. The stress components σ_y and σ_{xy} at a position 25 μm below the top surface are computed and plotted in Figs. 14 and 15 because these stress tensor components are zero on the surface.

4. Concluding Remarks

The integral-transformed solution of the elastodynamic equations involves integrals of highly oscillatory functions over semi-infinite intervals and inversion of a one-sided Laplace transform. The computational schemes employed are based on Filon's method and a Fourier-series technique for evaluating the numerical inversion of the Fourier-Laplace transform. As a disadvantage of the analytical model, we point out that the final inverse integral transforms have to be evaluated numerically which is more time consuming than the numerical schemes that solve for all the field points simultaneously. Thus the numerical model based on the finite element method is clearly capable of predicting the wave propagation phenomena, pulsed wave propagation, beam spread, and it has the ability to study arbitrarily shaped defects.

In the thermoelastic region of the laser ultrasonics, the thermal wave equation plays a key role in describing the source term. Since the speed of the Rayleigh surface wave is much slower than that of the heat wave, the temporal profile of the displacement is mainly determined by the material properties rather than by the laser-pulse properties. Therefore, it is very hard to broaden the frequency spectrum of the ultrasonic wave in the thermoelastic region. In an ablative regime, however, broad-band ultrasonic waves can be generated by using ultrashort laser pulses. A thermal dipole model can explain the physical process involved in generating the thermoelastic surface wave. The branch points and the real poles in the integral-transformed solution of the elastodynamic equations determine the arrival times of the compression, the shear, and the Rayleigh waves, respectively. The use of the Rayleigh surface wave may have a great advantage in NDT&E because it decays much less than the compression wave does with a distance.

References

Abramowitz, M. and Stegun, I. (1972) *Handbook of Mathematical Functions* (Dover, New York).

Burnett, D. S. (1987) *Finite Element Analysis: from Concepts to Applications* (Addison-Wesley, Reading).

Crump, K. S. (1976) Numerical Inversion of Laplace Transforms Using a Fourier Series Approximation, J. ACM, Vol. 22, pp. 89-96.

Durbin, F. (1974) Numerical Inversion of Laplace Transforms: An Efficient Improvement to Bubner and Abate's Method, Computer J., Vol. 17, pp. 371-376.

Frankel, J. I., Brian Vick and Ozisik, M. N. (1985) Flux Formulation of Hyperbolic Heat

Conduction, J. Appl. Phys., Vol. 58, pp. 3340-3345.

Kishore, N. N., Sridhar, I. and Iyengar, N. G. R. (2000) Finite Element modelling fo the Scattering of Ultrasonic Waves by Isolated Flows, NDT&E Int., Vol. 33, pp. 297-305.

Ozisik, M. N. and Brian Vick (1984) Propagation and Reflection of Thermal Waves in a Finite Medium, Int. J. Heat Mass Transfer, Vol. 27, pp. 1845-1854.

Reinhold Ludwig and William Lord (1988) A Finite Element Formulation for the Study of Ultrasonic NDT Systems, IEEE Trans. Ultrason. Ferroelectr. Frequency Control, Vol. 35, pp. 809-820.

Scruby, C. B. and Drain, L. E. (1990) *Laser Ultrasonics: Techniques and Applications* (Adam Hilger, Bristol).

Yoo, Jaegwon., Lim, C. H. and Baik, S. H. (2006) Thermoelastic Surface Waves Generated by Irradiation with a Line-Focused Laser Pulse, J. Korean Phys. Soc., Vol. 48, pp. 61-66.

Yoo, Jaegwon, Lim, C. H. and Kim, Cheoljung (2005) Numerical Study of Thermal Wave Propagating in a Disc Slab Irradiated by Ultrashort Laser Pulse, J. Korean Phys. Soc., Vol. 47, pp. 63-67.

Yoo, Jaegwon, Park, S. H., Jeong, Y. U., Lee, B. C. Rhee, Y. J. and Cho, S. O. (2004) A Numerical Study of the Integral Equations for the Laser Fields in Free-Electron Lasers, J. Korean Phys. Soc., Vol. 44, pp. 1407-1411.

Zerwer, A. M. Polak, A. and Santamarina, J. C. (2003) Rayleigh Wave Propagation for the Detection of Near Surface Discontinuities: Finite Element Modeling, J. Nondest. Eval., Vol. 22, pp. 39-52.